

Effective Field Theory search for High-Energy Nuclear Recoils using the XENON100 Dark Matter Detector

We report on WIMP search results in the XENON100 detector using a non-relativistic effective field theory approach. The data from science run II (34 kg * 224.6 live days) was re-analyzed, with an increased recoil energy interval compared to previous analyses, ranging from 6.6 to 240 keV. The data is found to be compatible with the background-only hypothesis. We present 90% confidence level exclusion limits on the coupling constants of WIMP-nucleon effective operators using a binned profile likelihood method. We also consider the case of inelastic WIMP scattering, where incident WIMPs may up-scatter to a higher mass state, and set exclusion limits on this model as well. Finally, we heuristically examine the dark matter search data above the maximum recoil energy of 240 keV considered in this analysis, and find no candidate nuclear recoil events.

Keywords: Dark Matter, EFT, Xenon

I. INTRODUCTION

Astrophysical and cosmological observations provide strong evidence that about 27% of the energy density of the universe is made out of Dark Matter (DM), a non-luminous, non-baryonic, and non-relativistic particle, the nature of which is yet unknown [1–3]. Many well-motivated theoretical extensions of the Standard Model of particle physics predict the existence of one or more particles with the required properties, with masses and cross sections typically of the order of the weak scale. Such particles are collectively known as Weakly Interacting Massive Particles (WIMPs) [4]. The hypothesis that dark matter is constituted primarily of WIMPs is currently being tested by many experiments, either indirectly by searching for evidence of their possible decay or annihilation in astrophysical processes, by searching for evidence of their direct production at collider experiments, or by directly measuring the rare scattering of astrophysical WIMPs from target nuclei in Earth-based laboratories [5–11]. We report on a search of this latter kind.

The traditional approach for computing predictions of the rate of WIMP-nucleon scattering has been to take only leading-order terms in a WIMP-nucleon effective field theory (EFT) with a very simple treatment of nuclear structure [12]. This leads to two main types of interactions, which are commonly labelled “Spin Independent” (SI) and “Spin Dependent” (SD). However, in recent years many authors have pointed out that in certain theories these interactions may be suppressed or nonexistent, such that otherwise subleading interactions may dominate the scattering process [13]. To account for this possibility in a systematic way, a more sophisticated EFT approach has been developed [14–16], in which an effective Lagrangian describing the WIMP-nucleus interaction is constructed that takes into account all Galilean-invariant operators up to second order in the momentum exchange. In this framework, new operators associated with different types of nuclear responses are introduced along with the standard SI and SD ones, resulting in a set of fourteen operators \mathcal{O}_i which may each couple independently to protons and neutrons. In Eqs. (1) we

list these operators following the convention from [15]. The operators depend explicitly on 4 linearly independent quantities: $\vec{v}^\perp \equiv \vec{v} + \frac{\vec{q}}{2\mu_N}$, the relative perpendicular velocity between the WIMP and the nucleon, \vec{q} , the momentum transferred in the scattering event, and \vec{S}_χ , \vec{S}_N , the WIMP and nucleon spins. \mathcal{O}_2 is not considered here as it cannot be obtained from a relativistic operator at leading order.

$$\begin{aligned}
\mathcal{O}_1 &= 1_{\chi 1_N} & \mathcal{O}_9 &= i\vec{S}_\chi \cdot (\vec{S}_N \times \frac{\vec{q}}{m_N}) \\
\mathcal{O}_3 &= i\vec{S}_N \cdot (\frac{\vec{q}}{m_N} \times \vec{v}^\perp) & \mathcal{O}_{10} &= i\vec{S}_N \cdot (\frac{\vec{q}}{m_N}) \\
\mathcal{O}_4 &= \vec{S}_\chi \cdot \vec{S}_N & \mathcal{O}_{11} &= i\vec{S}_\chi \cdot (\frac{\vec{q}}{m_N}) \\
\mathcal{O}_5 &= i\vec{S}_\chi \cdot (\frac{\vec{q}}{m_N} \times \vec{v}^\perp) & \mathcal{O}_{12} &= \vec{S}_\chi \cdot (\vec{S}_N \times \vec{v}^\perp) \\
\mathcal{O}_6 &= (\vec{S}_\chi \cdot \frac{\vec{q}}{m_N})(\vec{S}_N \cdot \frac{\vec{q}}{m_N}) & \mathcal{O}_{13} &= i(\vec{S}_\chi \cdot \vec{v}^\perp)(\vec{S}_N \cdot \frac{\vec{q}}{m_N}) \\
\mathcal{O}_7 &= \vec{S}_N \cdot \vec{v}^\perp & \mathcal{O}_{14} &= i(\vec{S}_\chi \cdot \frac{\vec{q}}{m_N})(\vec{S}_N \cdot \vec{v}^\perp) \\
\mathcal{O}_8 &= \vec{S}_\chi \cdot \vec{v}^\perp & \mathcal{O}_{15} &= -(\vec{S}_\chi \cdot \frac{\vec{q}}{m_N}) \left[(\vec{S}_N \times \vec{v}^\perp) \cdot \frac{\vec{q}}{m_N} \right] \quad (1)
\end{aligned}$$

Unlike the more commonly studied types of interaction (SI,SD), which are not suppressed when $\vec{q} \rightarrow 0$ and for which the scattering rate on nucleons is expected to be largest for low energy nuclear recoils, some of the new EFT operators depend explicitly on \vec{q} and so their interaction cross section is suppressed for low momentum transfers. Consequently, their scattering rate peaks at non-zero nuclear recoil energy. For sufficiently high WIMP masses, this may even occur outside typical analysis windows (< 43 keV) which are designed to search for SI and SD interactions (see Figure 1). Due to the theoretical bias of only considering SI and SD interactions, high energy nuclear recoils remain unexplored in many experiments.

Another typical assumption that can be relaxed is that WIMPs should scatter elastically with nuclei. However, there exist dark matter models in which the incoming and outgoing WIMPs have different mass states [17] separated by a keV-scale splitting. In the case where

73 the outgoing state is more massive than the incoming
 74 state, the cross section for low recoil energies can again
 75 be suppressed, this time by scattering kinematics. Re-
 76 cently an inelastic adaptation of the EFT operator frame-
 77 work discussed above was developed [18]. In this case
 78 the operators presented in Eqs. 1 are modified such that
 79 $\vec{v}_{inelastic}^\perp = \vec{v}_{elastic}^\perp + \frac{\delta_m}{|\vec{q}|^2} \vec{q}$. We consider this case in sec-
 80 tion III C 2.

81 The EFT framework of [14] is constructed at the
 82 WIMP-nucleon level and so each operator may be present
 83 independently for protons and neutrons, though UV
 84 models can of course correlate their couplings. The full
 85 EFT thus has 28 coupling parameters in addition to the
 86 WIMP mass (plus a mass splitting δ in the inelastic case).
 87 This parameter space is too large to explore in full, so we
 88 take a similar approach to the SI/SD case and character-
 89 ize the experimental limit by assuming only one active
 90 operator at a time, with the coupling to protons and neu-
 91 trons for that operator set equal (the “isoscalar” case).
 92 However, to facilitate the full exploitation of these results
 93 by the community, we provide in supplementary material
 94 a set of tools for converting any theoretical recoil spec-
 95 trum dR/dE into an accurate event rate prediction for
 96 this analysis, including all detector response and analysis
 97 efficiency effects. This may help to set a mildly conserva-
 98 tive but quite accurate limit on arbitrary models in the
 99 full EFT parameter space, or indeed any other particle
 100 dark matter model for which one can supply the expected
 101 recoil spectrum.

102 In this paper, motivated by these EFT extensions of
 103 the standard WIMP framework, we report on an anal-
 104 ysis extending the searched recoil energy range up to
 105 240 keV for the first time in the XENON100 experiment,
 106 and present exclusion limits on all operators for both the
 107 elastic and the inelastic WIMP cases.

II. THE XENON100 DETECTOR

109 The XENON100 detector is a cylindrical dual-phase
 110 xenon (liquid and gas) time projection chamber (TPC).
 111 It is installed at the Laboratori Nazionali del Gran
 112 Sasso (LNGS) in Italy and contains 161 kg of liquid
 113 xenon (LXe), of which 62 kg function as the active target
 114 [19]. The detector uses of a total of 178 1-inch square
 115 Hamamatsu R8520-AL photomultiplier tubes (PMTs)
 116 employed in two arrays, one in the gas phase at the top
 117 of the TPC, and the other at the bottom, immersed in
 118 the LXe.

119 A particle interacting with the LXe deposits energy
 120 that creates both prompt scintillation (S1) and delayed
 121 proportional scintillation (S2) which are detected using
 122 the two PMT arrays. The S2 signal is produced by ion-
 123 ized electrons, drifted in an electric field of 530V/cm to-
 124 wards the liquid-gas interface, where they are extracted
 125 using a stronger electric field of $\sim 12\text{kV}/\text{cm}$ to the gas
 126 phase in which the proportional scintillation occurs. The
 127 spatial distribution of the S2 signal on the top PMT ar-

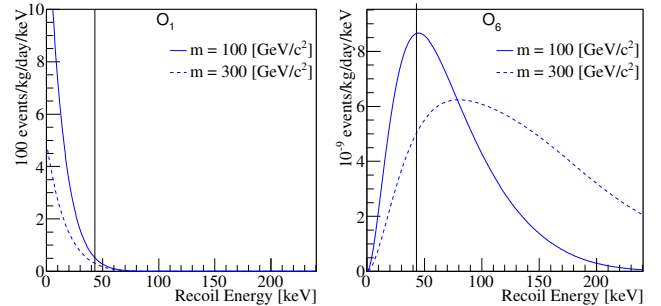


FIG. 1. Example EFT recoil spectra for elastic scattering of spin-1/2 WIMPs on Xenon nuclei (weighted according to the isotope abundances in the XENON100 experiment). Left(right) shows the predicted spectra for EFT operator $O_1(O_6)$. The normalization is controlled by the coupling coefficient of each EFT operator and the experimental exposure. The solid vertical line at 43 keV shows the approximate division between the two signal regions used in this analysis (30 PE in cS1). As shown, the standard SI (O_1) spectrum is concentrated mainly in the already-explored energy region. However, some EFT operators, for certain WIMP masses, predict a significant fraction of recoil events above the upper energy cut used in the standard spin-independent analysis, motivating an extension of this cut. The highest recoil energy shown in the plots, 240 keV, roughly corresponds to the extended cS1 cut of 180 PE used in this analysis.

128 ray, together with the time difference between $S1$ and
 129 $S2$ signals, provide respectively X-Y and Z position in-
 130 formation for each interaction, allowing 3D position re-
 131 construction to be achieved.

132 Interaction in different locations in the detector have
 133 different signatures. In order to take these effects into ac-
 134 count, a correction is applied based on light and charge
 135 collection efficiency maps. These maps are prepared us-
 136 ing calibration sources ranging up to energies well above
 137 240keV_{nr}, which is the highest energy recoil considered in
 138 this paper. The corrected signals (cS1,cS2) are spatially
 139 independent and uniform to all interactions [19]. Note
 140 that some of the top PMTs saturate for large S2 signals
 141 and we therefore use in this analysis only the bottom
 142 PMT array to infer the energy scale in S2.

143 The $S2/S1$ ratio is known to differ between nuclear re-
 144 coil (NR) and electronic recoil (ER) interactions, and is
 145 thus used as a discriminating variable between a WIMP
 146 signal and ER background. The logarithm of this ratio,
 147 $\log(cS2_b/cS1)$ is referred later in the text as the discrim-
 148 inating y variable.

III. DATA ANALYSIS

149 In this work we re-analyze science run II data recorded
 150 between February 2011 and March 2012, corresponding
 151 to 224.6 live days. The characterization of the detector
 152 response to ER interactions is performed using dedicated
 153 calibration campaigns with ^{60}Co and ^{232}Th radioactive

155 sources, while the response to NR interactions is performed using $^{241}\text{AmBe}$ calibration campaigns.
 156

157 This work extends the previous results [5, 20], referred
 158 to in the following as the low-energy channel, with a
 159 new study exploring the recoil energy range between 43-
 160 240 keV. The data analysis is divided into two mutually
 161 exclusive channels, one optimized for low energies and
 162 ranging from 3-30 PE in cS1(low-energy), the other opti-
 163 mized for high energies recoils ranging from 30-180 PE in
 164 cS1(high-energy). These two analyses are then combined
 165 statistically.

166 A. Low Energy Channel

167 This analysis channel relies on the re-analysis of run II
 168 data described in [5]. The ROI, the background expec-
 169 tation models, data selections and their acceptances are
 170 mostly unchanged and so are only briefly summarized
 171 here. Differences with respect to said results are high-
 172 lighted when present.

173 The region of interest for this channel spans the ROI
 174 in the $(y, \text{cS1})$ -plane and is shown in Figure 2. The lower
 175 bound on y corresponds to a 3σ acceptance quantile (as
 176 a function of cS1) of a 20 GeV WIMP mass signal model
 177 assuming an \mathcal{O}_1 (SI) interaction, while the upper bound
 178 is fixed at $y = 2.7$. The range in cS1 is selected as 3
 179 to 30 PE. This ROI is further divided into sub-regions
 180 dependent on each WIMP mass and operator (also called
 181 bands). These are arranged to achieve constant expected
 182 signal density in each region, as described in [5].

183 Other than falling into the ROI, an event should fulfill
 184 several additional selection criteria (cuts). Data qual-
 185 ity and selection cuts are defined to remove events with
 186 poor data quality or noisy signals, a time-coincident sig-
 187 nal in the outer LXe veto, S2 signals below threshold,
 188 multiple-scatters, and positions outside a predefined fidu-
 189 cial volume of 34 kg. In addition, this analysis channel
 190 uses the post-unblinding cuts and data reprocessing de-
 191 scribed in [5]. More details on these selection criteria and
 192 their relative WIMP signals acceptances can be found
 193 in [5, 21].

194 To summarize the main new features in this analysis,
 195 data is reprocessed with an improved (S1,S2) classifica-
 196 tion algorithm, and a new cut targeted to suppress data
 197 periods with non-random occurrence of lone-S1 (an S1
 198 without any correlated S2) events is applied. Finally,
 199 this channel does not employ a variable lower S1 thresh-
 200 old as a function of the event position in the TPC, but
 201 a fixed lower threshold cut on cS1 at 3 PE, converse to
 202 what was done in [5].

203 The expected background is modeled separately for ER
 204 and NR contributions which are then scaled to exposure
 205 and added together. The NR background is estimated
 206 by Monte Carlo simulation and accounts for the radio-
 207 genic and cosmogenic neutron contributions [22]. The
 208 ER background is parametrized as the linear combina-
 209 tion of Gaussian-shaped and non-Gaussian components.

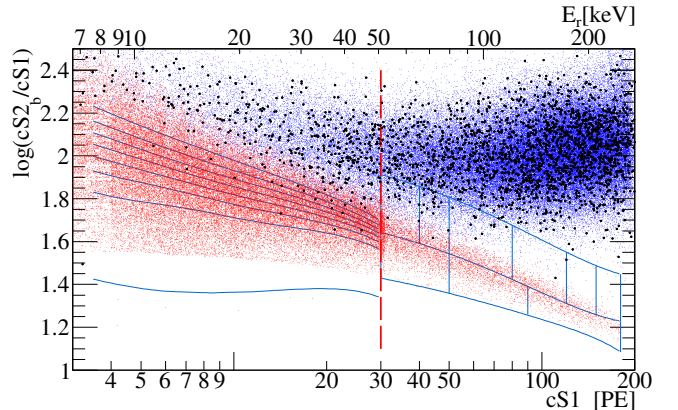


FIG. 2. Summary of regions of interest, backgrounds, and observed data. ER calibration data, namely ^{60}Co and ^{232}Th data is shown as blue dots. NR calibration data ($^{241}\text{AmBe}$) is shown as red dots. Dark matter search data is shown as black dots. The red dashed line is the threshold between the low and high energy channels. The lines in blue are the bands. For the low-energy channel these are operator and mass dependent, but are shown here for a 50 GeV/c^2 WIMP using the \mathcal{O}_1 operator. For the high-energy region, the 9 analysis bins are presented; the top left bin in this region is bin 1, the top right is bin 6, the bottom left is bin 7 and bottom right is bin 9. In Appendix A we show similar data but for regions above the upper range of this analysis, going up to 1000 PE in cS1, for completeness as part of final unblinding of XENON100 data.

210 The first is obtained via a parametric fit of the ^{60}Co and
 211 ^{232}Th calibration data, as discussed in [20]. In contrast,
 212 the expected distribution and yields for the non-Gaussian
 213 population, consisting of anomalous events such as those
 214 presenting incomplete charge collection or accidental co-
 215 incidence of uncorrelated S1s and S2s, are evaluated via
 216 dedicated techniques described in [5].

217 Systematic uncertainties on the background model
 218 arising from the Gaussian parametrized fit plus the nor-
 219 malisations of the NR and non-Gaussian components
 220 have been evaluated and propagated to each band. These
 221 errors are small with respect to the statistical uncertain-
 222 ties of each band, which are taken as the overall uncer-
 223 tainty [5] as discussed in Sec. III D.

224 B. High Energy Channel

225 This analysis channel targets high energy nuclear re-
 226 coils and is the focus of this work. The data selection
 227 criteria we use are based on the criteria described in de-
 228 tail in [21], which were optimized for high acceptance to
 229 low energy nuclear recoils. Most of these cuts were found
 230 to be fully compatible with (or easily extended) to high
 231 energy depositions, however some required more compre-
 232 hensive studies, which are described in the following.

233 The width of an S2 pulse increases with the depth (z)
 234 of the interaction. This is due to the diffusion of the
 235 electron cloud during its propagation through the liquid

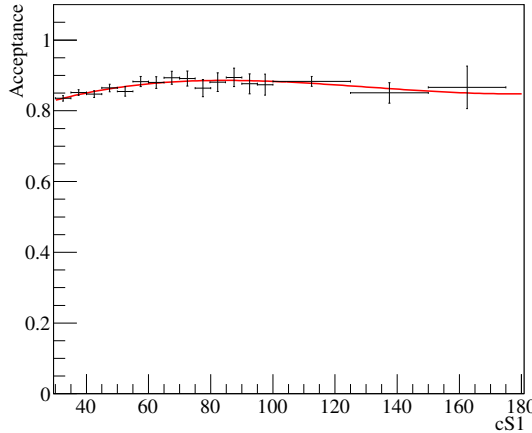


FIG. 3. The total acceptance of all cuts used. Data from calibration is shown in black, with a 3rd order polynomial fit in red.

xenon. since low energy S2 events show larger spread due to low statistics of drifted electrons, the cut was previously defined in an energy-dependent way. However, for the large recoil energies considered in this channel, this energy dependency is no longer valid. We therefore use here a cut on the S2 width which is a function of the depth of the interaction alone.

As a WIMP will interact only once in the detector, we remove events which have more than one S2. We adopt here a cut that is more suitable to higher energies and demand a single S2 in a $160 \mu\text{s}$ window, instead of a linear dependence between the second S2 size and the first.

To define the interaction's exact location in (x, y) , we use several algorithms, one of which is based on a Neural Network (NN) [21]. The NN was not trained to recognize high energy ER events and therefore a cut on the NN reconstruction quality is not suitable for this analysis. We therefore discard this cut but keep all other cuts on position reconstruction quality, which is sufficient to ensure a correct position reconstruction.

The total acceptance to WIMP signals is computed based on $^{241}\text{AmBe}$ calibration data as a function of cS1, following the procedure described in [21]. We present this function in Figure 3, where the total acceptance is fitted using a third order polynomial.

We define our signal region in the discrimination $(y, \text{cS1})$ -plane using $^{241}\text{AmBe}$ calibration data. The region of interest (ROI) is shown in Figure 2 as blue contour lines. The upper bound is defined such that the contribution due to xenon excitation lines is negligible. The lower bound is defined as the 3σ acceptance quantile of the $^{241}\text{AmBe}$ distribution.

We divide our signal region into two bands in y , constructed such that the $^{241}\text{AmBe}$ data sample is equally distributed in between them. The total number of events in each band is ~ 3000 events. The bands are further di-

#	Band	Energy Range (cS1)	# Background Events	# Data Events
1	upper	30 - 40	23.5	20
2	upper	40 - 50	15.7	17
3	upper	50 - 80	12.4	11
4	upper	80 - 120	1.1	1
5	upper	120 - 150	0.1	1
6	upper	150 - 180	0.08	0
7	lower	30 - 50	0.9	0
8	lower	50 - 90	0.35	0
9	lower	120 - 180	0.18	0

TABLE I. Definitions and contents of the analysis bins for the high energy channel. The expected background counts are calculated by taking the calibration sample and scaling it by 6.54×10^{-3} , which is the ratio of observed counts to calibration counts in a sideband.

vided into nine bins. The definition and content of the bins are presented in Table I and in Figure 2.

The main source of background results from ER leakage. We therefore estimate the background distribution in the ROI using ^{60}Co and ^{232}Th calibration events. Contributions from radiogenic and cosmogenic neutrons, as well as accidental coincidence, are negligible for such a high energy recoil. In Table I we report the background expectation for each bin in the ROI along with the observed events in each bin. Here the background expectation is computed by scaling the calibration sample yield by 6.54×10^{-3} , which is simply the ratio of observed counts to calibration counts in an independent sideband. The sideband is defined above the upper limit of this analysis and below the ER calibration band mean. Note that in the computation of exclusion limits the background normalization is instead fitted to data during hypothesis testing, rather than using the sideband normalization, as described in section III D.

C. Signal Model

The signal model is produced by taking a theoretical event rate spectrum, the production of which is described in sections III C 1 and III C 2, and applying the analysis acceptance and detector response as described in [21] to obtain the expected event rate in the detector in terms of detector variables (i.e. $\text{cS1}, \text{cS2}_b$). In order to calculate the expected value of the signal in cS1 , we use Eq. 2 for both energy regions,

$$\langle \text{cS1} \rangle = E_{\text{nr}} \cdot (L_y \mathcal{L}_{\text{eff}}) \cdot \left(\frac{S_{\text{nr}}}{S_{\text{ee}}} \right) \quad (2)$$

where E_{nr} is the recoil energy, L_y is the average light yield in the detector, \mathcal{L}_{eff} is the scintillation efficiency relative to $122\text{keV}_{\text{ee}}$ as a function of E_{nr} , and S_{ee} and S_{nr} are the quenching factors due to the externally applied electric field. Aside from E_{nr} and \mathcal{L}_{eff} these parameters have fixed values, namely $L_y = 2.28 \pm 0.04$, $S_{\text{nr}} = 0.95$,

and $S_{ee} = 0.58$. Recoils below 3 keV are assumed to produce no light since \mathcal{L}_{eff} is not measured at these energies. For details of the physics behind these parameters and the construction of the signal PDF see [5, 21].

The expected cS2 signal is computed following [23] using Eq. 3 for the low-energy region only,

$$\langle \text{cS2}_b \rangle = E_{\text{nr}} Q_y Y \quad (3)$$

where $Y = 8.27 \pm 0.26$ is the amplification factor determined from the detector response to single electrons [24], and Q_y is the charge yield as a function of E_{nr} . Applying the detector and PMT responses, and the acceptance as in [5], defines the low-energy signal model over the region $3\text{PE} < \text{cS1} < 30\text{PE}$, with $\text{cS2}_b > 73.5\text{PE}$ as the S2 threshold.

Eq. 3 hides a subtlety. The actual cS2_b PDF is composed of two pieces, a Poisson term associated with the initial charge liberation and a Gaussian term associated with the PMT response and other detector effects:

$$p_{\text{S2}}(\text{cS2}_b | E) = \sum_{N'} P_{\text{pmt}}(\text{cS2}_b | Y N', \sigma_Y \sqrt{N'}) \cdot \text{Pois}(N' | \mu_Q) \quad (4)$$

where $\mu_Q = E_{\text{nr}} Q_y$ is the expected number of liberated charges in a nuclear recoil event of energy E , and N' is the actual number of liberated charges, which are unmeasured and thus summed over. The amplification factor Y is applied to the actual number of liberated charges N' , not the expected number μ_Q . Associated with this is the variance of the Gaussian response PDF, $\sigma_Y \sqrt{N'}$, where in this analysis $\sigma_Y = 6.93$ as measured and described in [24].

For the high energy region we cannot produce the S2 distribution in the same way as the method in [23] has not been calibrated for such high recoil energies. We therefore use the NR calibration data distribution in $\log(\text{cS2}_b/\text{cS1})$ to estimate the WIMP distribution. Above 180PE in cS1, the statistics of $^{241}\text{AmBe}$ data is too low to estimate the distribution accurately. This forms the higher bound of this analysis. With the cS2_b distribution determined by this empirical method, we require only a prediction of the cS1 distribution. This is obtained from Equation (2), followed by the application of detector and PMT responses, as well as the acceptance given in Figure 3, which completes the high-energy signal model definition.

Examples of each for two EFT operators are shown in Figures 4 and 5, with the rate normalized to give 5 events in the total energy range (low-energy and high-energy).

1. Elastic Scattering

The expected recoil energy spectrum of each WIMP mass for each EFT operator is calculated using the Mathematica package `DMFormFactor` supplied by Anand et al. [15, 16]. We use standard assumptions as in previous analyses (e.g [5]) regarding the local dark matter density

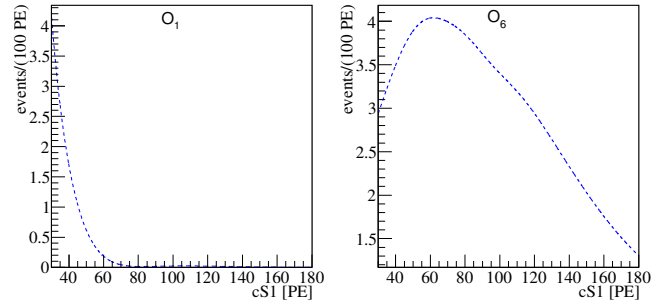


FIG. 4. The expected signal in the high energy region for a 300 GeV/c^2 WIMP mass, normalized to 5 events. Left(right) is the spectra for $O_1(O_6)$. Notice that for O_1 most of the events are not expected to deposit energy higher than 30 PE whereas for O_6 a large fraction of the events appear in this region.

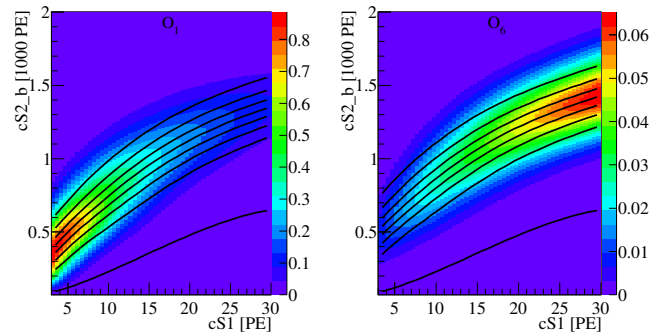


FIG. 5. The expected signal in the low energy region for a 300 GeV/c^2 WIMP mass, normalized to 5 events. Left(right) is the spectra for $O_1(O_6)$. Notice that for O_1 most of the events are expected to deposit energy lower than 30 PE whereas for O_6 a large fraction of the events do not appear in this region at all. The black lines indicate the bands constructed on these specific mass and operator models, and are dividing the signal into 8 equally distributed signal sub-regions. This parameter space can be mapped with a one to one mapping to the $y - \text{cS1}$ space.

and velocity distribution, namely $\rho_{\text{local}} = 0.3 \text{ GeV/cm}^3$ and a Maxwell-Boltzman distribution with a mean given by the local circular velocity $v_0 = 220 \text{ km/s}$ and cut off at an escape velocity of $v_{\text{esc}} = 544 \text{ km/s}$. The responses of xenon nuclei to a scattering event are computed from one-body density matrices provided with the `DMFormFactor` package, in contrast to the Helm form factors which have been used in previous analyses. These spectra are produced for the seven most abundant xenon isotopes (128,129,130,131,132,134 and 136), combined in proportion to the abundance of these isotopes in the XENON detector [25], then translated into expected signal rates via the method described above.

369

2. Inelastic WIMP Scattering

To obtain recoil spectra for WIMP-nucleon scattering for all EFT operators with inelastic kinematics, we use a modified version of `DMFormFactor` provided by Barella et. al. [18]. The authors have modified the original package to enforce the new energy conservation condition $\delta_m + \vec{v} \cdot \vec{q} + |\vec{q}|^2 / 2\mu_N = 0$, primarily by replacing $\vec{v}_{\text{elastic}}^\perp \rightarrow \vec{v}_{\text{inelastic}}^\perp = \vec{v}_{\text{elastic}}^\perp + \frac{\delta_m}{|\vec{q}|^2} \vec{q}$ in the definitions of the EFT and nuclear operators, giving rise to the well-known minimum velocity for scattering

$$v_{\min}/c = \frac{1}{\sqrt{2m_N E_R}} \left| \frac{m_N E_R}{\mu_N} + \delta_m \right| \quad (5)$$

where μ_N is the WIMP-nucleon reduced mass.

Assumptions regarding the dark matter halo and nuclear physics are unchanged. The mass splitting δ_m between dark matter states is varied from 0 to 300 keV, safely beyond the value at which the predicted rate is zero for the entire mass range we consider.

385

D. Statistical Inference

The statistical interpretation of data is performed by means of a binned profiled likelihood method, in which hypothesis testing relies upon a likelihood ratio test statistic, \tilde{q} , and its asymptotic distributions [26]. The two analysis channels are statistically independent once certain common nuisance parameters are factored out, we therefore combine them by multiplying their likelihoods together to produce a joint likelihood. Both analyses parametrize the NR relative scintillation efficiency, \mathcal{L}_{eff} , based on existing measurements [27]. Its uncertainty is the major contributor to energy scale uncertainties and is considered as correlated between the two analysis channels via a separate nuisance likelihood term. Throughout this study, all the parameters related to systematic uncertainties are assumed to be normally distributed.

For the low energy channel an extended likelihood function is employed which is very similar to the one reported in [28] and described in detail in [5]. The ROI discriminating $(y, cS1)$ -plane is divided into eight WIMP mass dependent bands where events are counted. This binned approach is extended with the corresponding $cS1$ -projected probability density function of each band. The total normalization of the background is fit to data, and an uncertainty is assigned to the relative normalization of each band according to the corresponding statistical uncertainty of the calibration sample. Signal shape variations due to energy scale uncertainty are modeled via simulation. Additionally to \mathcal{L}_{eff} , uncertainties due to the charge yield function Q_y are parametrized as described in [23].

The high energy channel analysis employs a binned likelihood function. Observed and expected event yield are compared in the nine ROI $(y, cS1)$ -bins described in

section III B. Given the large statistical uncertainty of the background model the above extended likelihood approach is not repeated here. Instead, the maximum likelihood estimation of the background expectation in each bin is constrained by the statistical uncertainty of the calibration sample, while the total normalization is fit to the data. Additionally, to account for potential mismodeling of the expected background distribution, mainly due to anomalous multiple scatter events, a systematic uncertainty of 20% is assigned independently to each bin. In this channel (high energy), uncertainty on the signal acceptance of analysis selections are computed for each signal hypothesis using the parametrized acceptance curve shown in Figure 3. Uncertainties on the signal model ($y, cS1$) distribution due to $^{241}\text{AmBe}$ sample statistical fluctuations, as well as energy scale shape variation due to \mathcal{L}_{eff} uncertainties, are taken into account.

436

IV. RESULTS

A benchmark region of interest is defined between the upper and lower thresholds in $cS1$ for each channel. This region is bounded in y -space from above by the $^{241}\text{AmBe}$ NR mean line and below by the lower 3σ quantile of the $^{241}\text{AmBe}$ neutron calibration data. The expected background in the region is 3 ± 0.5 (low-energy) and 1.41 ± 0.28 (high-energy). The number of DM candidates in this benchmark region is 3 (low-energy), and 0 (high-energy). The data is compatible with the background-only hypothesis and no excess is found.

For the elastic scattering case, a 90% CL_S [29] confidence limit is set on the effective coupling constant, c_i , for all operators and masses in the range of $10 \text{ GeV}/c^2$ to $1 \text{ TeV}/c^2$. The c_i are dimensionful, with units of $[\text{mass}]^{-2}$, so we first convert them to dimensionless quantities by multiplying them by $m_{\text{weak}}^2 = (246.2 \text{ GeV})^2$, following the conventions of [15]. These limits are shown in Fig. 7 in black, along with limits from CDMS-II Si, CDMS-II Ge and SuperCDMS [30].

As explained in Sec. III, the upper boundary in $cS1$ of our search region is set at 180 PE due to a lack of NR calibration data above this, however we heuristically examined a range of up to 1000 PE, and found no NR candidates in that region. Due to the lack of calibration data in this energy regime we cannot use this observation to set any limits, however this could be done once calibration data becomes available.

For the inelastic scattering case, 90% CL_S confidence limits on the coupling constants (again scaled by m_{weak}^2) are set. Fig. 6 shows limits on the \mathcal{O}_1 (SI) coupling constant as a function of mass splitting and WIMP mass, Fig. 8 shows limits for all other operators as a function of the mass splitting δ_m with a fixed WIMP mass of $1 \text{ TeV}/c^2$.

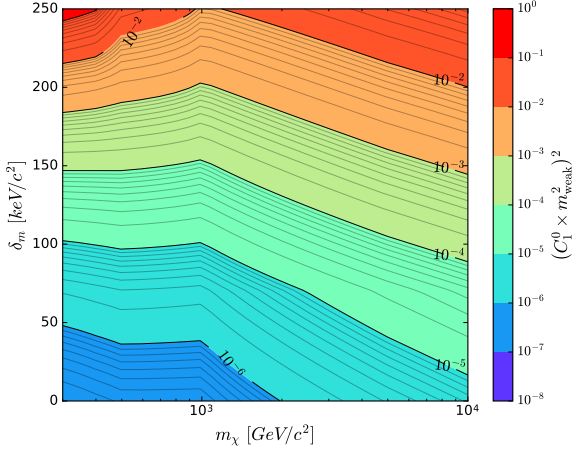


FIG. 6. 90% CL_S limits, for the inelastic model, on the magnitude of the coupling constant for \mathcal{O}_1 , reported as a function of the WIMP mass and mass splitting δ .

472

V. SUMMARY

473 We have shown the first analysis of XENON100 data
 474 at recoil energies above 43 keV, with the new high energy
 475 bound set to 240 keV. We considered in this paper two
 476 models which predict interactions in this energy region:
 477 an EFT approach for elastic WIMP-nucleon scattering,
 478 and a similar EFT approach but considering instead in-
 479 elastic WIMP-nucleon scattering. The observed data was
 480 compatible with background expectations, and 90% CL_S
 481 exclusion limits were constructed for WIMP masses be-
 482 tween 10-1000 GeV. An even higher energy range, up to
 483 1000 PE in cS1, was examined without statistical analy-
 484 sis, with no candidate NR events found.

485

VI. ACKNOWLEDGMENT

486 Liam Fitzpatrick Spencer Chang

Appendix A: Data from recoil energies up to 1000 PE

487 This analysis is focused on energy recoils up to 240 keV
 488 (180 PE) due to low statistics of NR calibration data at
 489 higher energies. However, for completeness, we present
 490 the data for events with recoil energies up to 1000 PE
 491 in 9. The data selection criteria are the same as those
 492 applied for the high-energy analysis region. The dark
 493 matter data is heuristically seen to be compatible with
 494 the ER calibration data, with no clear abnormalities seen,
 495 implying the absence of candidate nuclear recoil events.

498 Appendix B: Signal model detector response table

499 In this appendix we describe digital tables which can
 500 be used to construct an accurate signal model for this
 501 analysis given any input recoil spectrum dR/dE arising
 502 from a theoretical model. A visualization of the tables
 503 is shown in Fig. 10, and in section B 1 we show a sim-
 504 ple example Python code of how to use the supplied ta-
 505 bles. Currently we provide these tables only for the high-
 506 energy analysis region.

The signal model for the high-energy analysis region
 can be expressed analytically in the form:

$$\frac{dR}{dcS1} = \int \frac{dR}{dE} \cdot \epsilon_{S1}(cS1) \cdot \epsilon_{S2'}(E) \cdot p_{S1}(cS1|E) dE \quad (B1)$$

$$= \int \frac{dR}{dE} G(cS1, E) dE \quad (B2)$$

507 where $\epsilon_{S1}(cS1)$ and $\epsilon_{S2'}(E)$ represent analysis cut effi-
 508 ciencies, $p_{S1}(cS1|E)$ encodes detector effects, and dR/dE
 509 gives the theoretically predicted nuclear recoil rate from
 510 WIMP scattering. In the second line we emphasize that
 511 all the detector and analysis effects can be encoded in a
 512 single function $G(cS1, E)$. To make a signal prediction
 513 for the bins in our analysis, this expression needs to be
 514 integrated over the appropriate range of $cS1$ for each bin
 515 (and divided by two to account for the banding structure
 516 in $cS2_b$):

$$R_{\text{bin}_i} = \frac{1}{2} \int_{\text{lower}_i}^{\text{upper}_i} \frac{dR}{dcS1} dcS1 \quad (B3)$$

With some simple rearrangement this rate can be written
 in terms of an integral over the detector response function
 G as follows

$$R_{\text{bin}_i} = \frac{1}{2} \int \frac{dR}{dE} \int_{\text{lower}_i}^{\text{upper}_i} G(cS1, E) dcS1 dE \quad (B4)$$

$$= \int \frac{dR}{dE} G'_i(E) dE \quad (B5)$$

517 where in the last line we absorb the factor of 1/2 into
 518 the definition of G'_i . We see here that the signal rate
 519 for each bin can be expressed as an integral over the re-
 520 coil spectrum times a detector response function G'_i for
 521 that bin. It is these detector response functions which
 522 are shown in Fig. 10, and which we provide digitally
 523 for use by the community. A low-resolution example is
 524 given in Table II. With these tables it is simple to pro-
 525 duce a signal model for our analysis for any theoretical
 526 recoil spectrum. The functions G'_i are provided for three
 527 values of the nuisance variable \mathcal{L}_{eff} , namely the median
 528 value and values at $\pm 1\sigma$ in \mathcal{L}_{eff} . From these, along with
 529 the measured background rates given in table I, one may
 530 construct a likelihood which accounts for uncertainties in
 531 \mathcal{L}_{eff} . Alternatively simply using the -1σ value produces
 532 quite an accurate prediction and is generally conserva-
 533 tive.

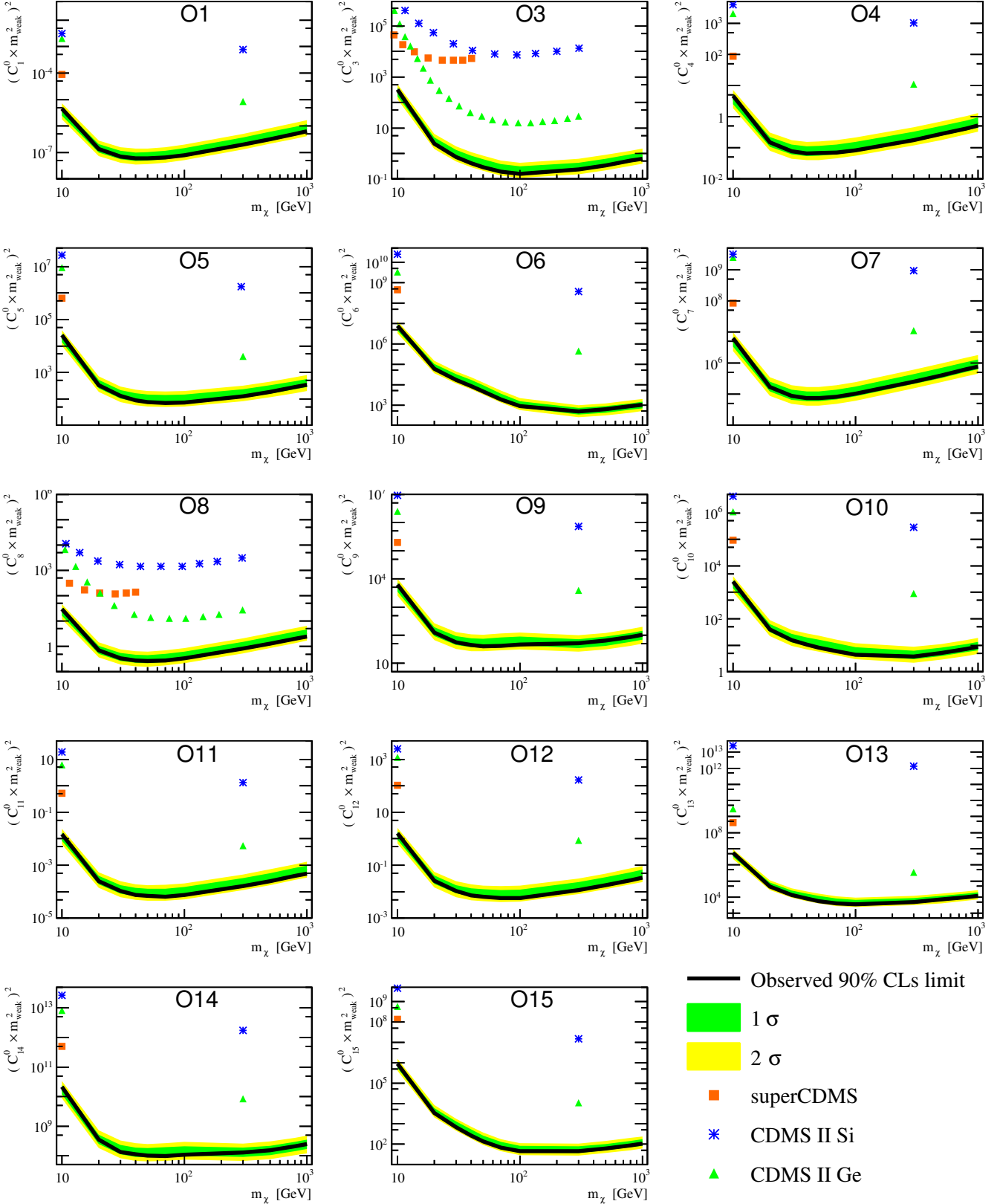


FIG. 7. The XENON100 limits (90% CL_S) on isoscalar dimensionless coupling for all elastic scattering EFT operators. The limits are indicated in solid black. The expected sensitivity is shown in green and yellow(1 σ and 2 σ respectively). Limits from CDMS-II Si, CDMS-II Ge, and SuperCDMS [30] are presented as blue asterisks, green triangles, and orange rectangles, respectively (color online). For operator 3 and 8 a full limit from CDMS is published and indicated by a dashed line in the respective colors.

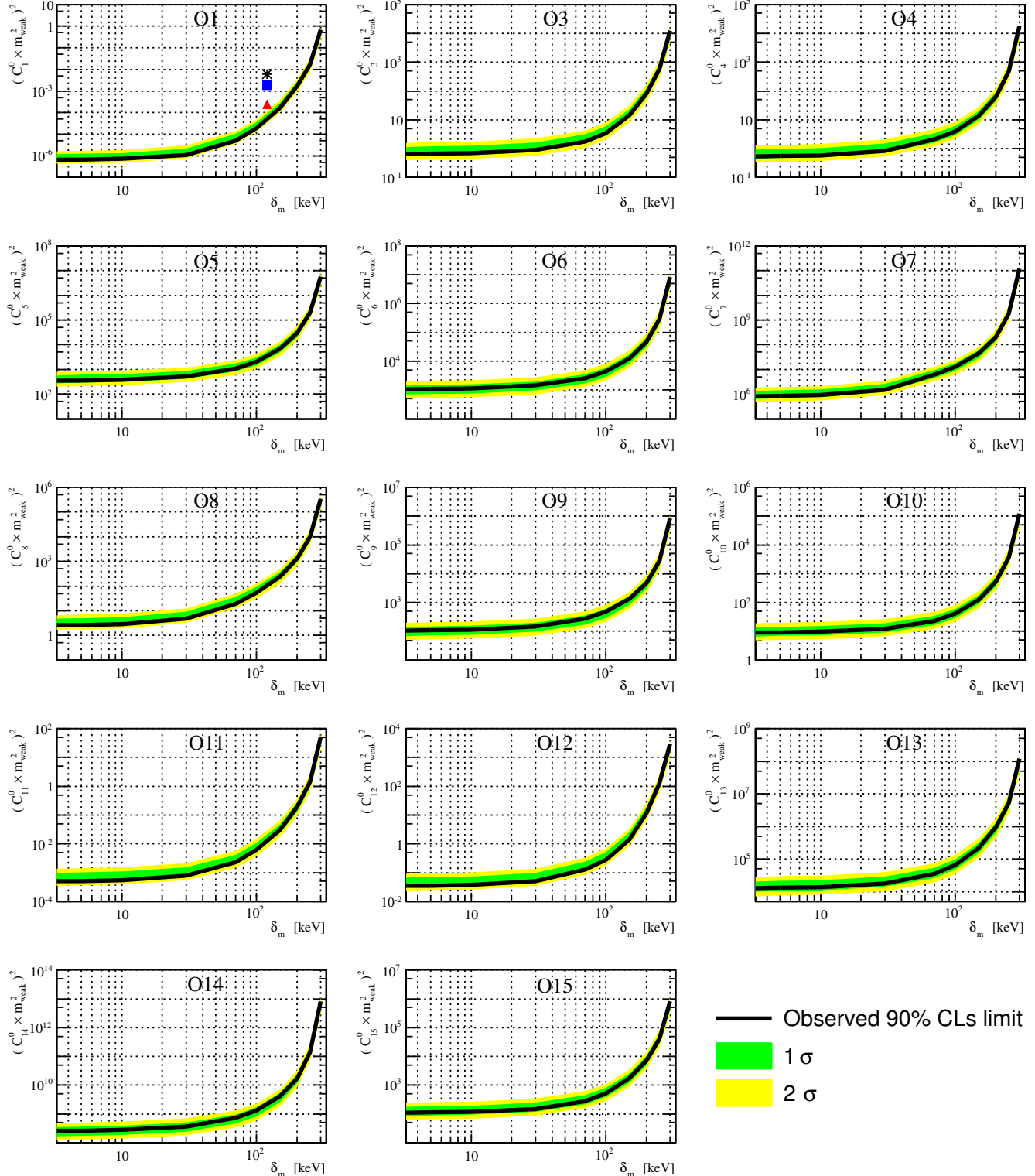


FIG. 8. The XENON100 90% CL_S limits on a $1 \text{ TeV}/c^2$ WIMP isoscalar dimensionless coupling as function of the WIMP mass splitting δ_m for all inelastic scattering EFT operators. Limits are indicated in solid black. The expected sensitivity is shown in green and yellow (1σ and 2σ respectively).

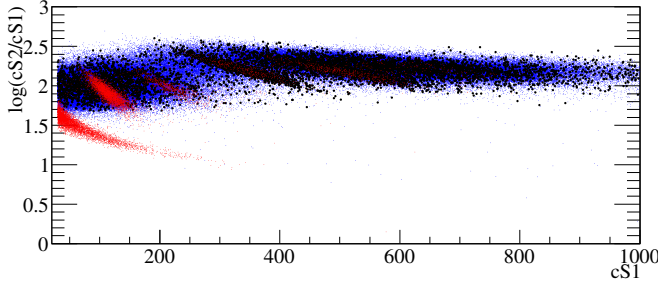


FIG. 9. The full dark matter search data for XENON100 up to 1000 PE in cS1 (shown in black). In blue we show data from ER calibration (^{60}Co and ^{232}Th). In red we show data from NR calibration ($^{241}\text{AmBe}$). The two large populations (in black) at 350 PE and 500 PE are the 110 keV and 197 keV excitation lines of ^{19}F coming from the PTFE walls of the TPC. No statistical analysis is possible for the data above about 180 PE in cS1, due to insufficient NR calibration sample statistics. However, from the trend of the calibration data and the lack of candidate events outside the ER band, we can heuristically claim to see zero candidate nuclear recoil events in the energy regime beyond our analysis.

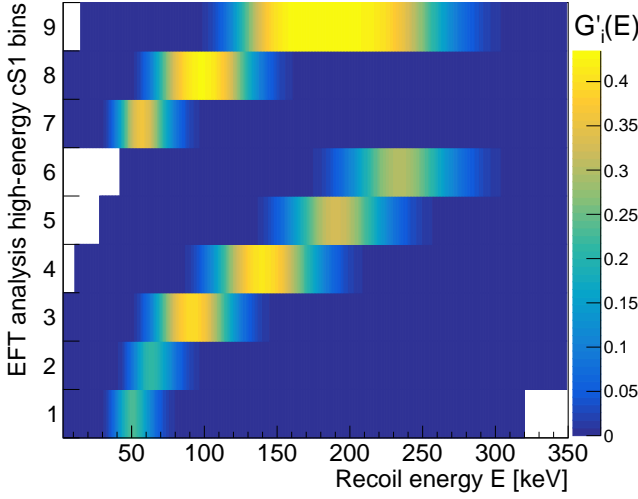


FIG. 10. A visualization of the detector response table for -1σ (i.e. conservative) \mathcal{L}_{eff} , as provided in the supplementary material. The table visualization shows, on the y axis, the bins used for the high-energy signal region of this analysis. The x axis shows recoil energies, and the colours give the probability density for a recoil of a given recoil energy to produce an event in each analysis bin. To produce a signal model for this analysis, one simply multiplies the table values by dR/dE and integrates over E . The result is the predicted signal rate for each analysis bin.

1. Example code

#	E(keV)	bin 1	bin 2	bin 3	bin 4	bin 5	bin 6	bin 7	bin 8	bin 9
3.00e+00	1.44e-22	2.70e-32	1.23e-42	0.00e+00	0.00e+00	0.00e+00	1.44e-22	1.23e-42	0.00e+00	0.00e+00
1.30e+01	9.21e-09	7.58e-14	1.25e-19	6.21e-40	0.00e+00	0.00e+00	9.21e-09	1.25e-19	0.00e+00	0.00e+00
2.30e+01	1.74e-04	1.07e-04	1.24e-11	1.51e-26	0.00e+00	0.00e+00	1.74e-04	1.24e-11	2.64e-32	3.30e+01
3.30e+01	2.22e-02	2.79e-04	6.55e-07	5.47e-18	8.20e-38	0.00e+00	2.25e-02	6.55e-07	1.71e-22	4.30e+01
4.30e+01	1.59e-01	1.68e-02	3.50e-04	1.89e-12	1.24e-28	1.82e-43	1.76e-01	3.50e-04	4.95e-16	5.30e+01
5.30e+01	2.23e-01	1.21e-01	1.40e-02	1.26e-08	6.89e-22	1.43e-34	3.44e-01	1.40e-02	1.82e-11	6.30e+01
6.30e+01	1.10e-02	2.12e-01	9.84e-02	4.73e-06	5.28e-17	5.47e-28	3.21e-01	9.84e-02	2.59e-08	7.30e+01
7.30e+01	2.77e-02	1.54e-01	2.51e-02	2.58e-04	2.20e-13	5.56e-23	1.82e-01	2.51e-01	4.20e-06	8.30e+01
8.30e+01	4.38e-04	6.14e-02	3.67e-03	4.07e-03	1.36e-10	5.26e-19	6.58e-02	3.71e-01	1.65e-04	9.30e+01
9.30e+01	4.65e-04	1.52e-02	3.96e-01	2.73e-02	2.31e-08	1.01e-15	1.57e-02	4.21e-01	2.44e-03	1.03e+02
1.03e+02	3.40e-05	2.47e-03	3.41e-01	9.81e-02	1.50e-06	6.05e-13	2.50e-03	4.21e-01	1.75e-02	1.13e+02
1.13e+02	1.91e-06	2.89e-04	2.29e-01	2.13e-01	4.09e-05	1.22e-10	2.91e-04	3.74e-01	6.77e-02	1.23e+02
1.23e+02	7.75e-08	2.38e-05	1.14e-01	3.28e-01	5.91e-04	1.16e-08	2.39e-05	2.76e-01	1.66e-01	1.33e+02
1.33e+02	2.18e-09	1.33e-02	3.98e-02	3.97e-01	5.03e-03	5.94e-07	1.33e-06	1.55e-01	2.87e-01	1.43e+02
1.43e+02	5.40e-11	6.21e-08	1.05e-02	4.06e-01	2.41e-02	1.42e-05	6.21e-08	6.64e-02	3.74e-01	1.53e+02
1.53e+02	1.33e-12	2.71e-09	2.23e-03	3.66e-01	7.14e-02	1.73e-04	2.71e-09	2.26e-02	4.17e-01	1.63e+02
1.63e+02	2.86e-14	1.00e-10	3.75e-06	2.85e-01	1.51e-01	1.32e-03	1.00e-10	6.04e-03	4.32e-01	1.73e+02
1.73e+02	5.43e-16	3.19e-12	5.09e-05	1.86e-01	2.43e-01	6.76e-03	3.19e-12	1.28e-02	4.34e-01	1.83e+02
1.83e+02	9.29e-19	8.90e-14	1.56e-06	1.01e-01	3.09e-01	2.42e-02	8.90e-14	2.21e-04	4.34e-01	1.93e+02
1.93e+02	1.44e-19	2.21e-15	5.32e-07	4.46e-02	3.23e-01	6.38e-02	2.21e-15	3.14e-05	4.31e-01	2.03e+02
2.03e+02	2.05e-21	4.92e-17	4.23e-08	1.62e-02	2.83e-01	1.29e-01	4.92e-17	3.73e-06	4.28e-01	2.13e+02
2.13e+02	7.71e-23	9.96e-19	2.91e-09	4.89e-03	2.10e-01	2.06e-01	9.96e-19	3.78e-07	4.21e-01	2.23e+02
2.23e+02	3.33e-25	1.85e-20	1.74e-10	1.23e-03	1.31e-01	2.71e-01	1.85e-20	3.29e-08	4.04e-01	2.33e+02
2.33e+02	3.83e-27	3.16e-22	9.25e-12	2.63e-02	6.94e-02	2.99e-01	3.16e-22	2.51e-01	3.69e-01	2.43e+02
2.43e+02	4.16e-29	5.03e-24	24.43e-13	4.80e-05	3.12e-02	2.81e-01	5.03e-24	1.68e-03	3.12e-01	2.53e+02
2.53e+02	4.29e-31	7.48e-26	1.87e-14	7.55e-06	1.20e-02	2.27e-01	7.48e-26	1.00e-11	2.39e-01	2.63e+02
2.63e+02	4.21e-33	1.05e-27	2.723e-16	1.04e-06	3.94e-03	1.58e-01	1.05e-27	5.38e-13	1.62e-01	2.73e+02
2.73e+02	3.95e-35	1.39e-29	2.56e-17	1.25e-07	1.12e-03	9.59e-02	1.39e-29	2.61e-14	9.70e-02	2.83e+02
2.83e+02	3.56e-37	1.74e-31	8.33e-19	1.34e-08	2.77e-04	5.04e-02	1.74e-31	1.15e-15	5.07e-02	2.93e+02
2.93e+02	3.08e-39	2.08e-35	3.25e-20	1.29e-09	6.00e-06	2.31e-02	2.08e-33	4.67e-17	2.31e-02	3.03e+02
3.03e+02	2.58e-41	2.38e-35	7.04e-22	1.11e-10	1.15e-05	9.25e-03	2.38e-35	1.75e-18	9.26e-03	3.13e+02
3.13e+02	2.03e-43	2.61e-37	1.84e-23	8.69e-12	1.95e-06	3.26e-03	2.61e-37	6.06e-20	3.26e-03	3.23e+02
3.23e+02	0.00e+00	2.76e-39	4.54e-25	6.20e-13	2.97e-07	1.01e-03	2.76e-39	1.96e-21	1.01e-03	3.33e+02
3.33e+02	0.00e+00	2.81e-41	1.05e-26	4.06e-14	4.06e-08	2.80e-04	2.81e-41	5.93e-23	2.80e-04	3.43e+02
3.43e+02	0.00e+00	2.72e-43	2.32e-28	2.44e-15	5.04e-09	6.91e-05	2.72e-43	1.69e-24	6.91e-05	

TABLE II. Detector response table using \mathcal{L}_{eff} with constrained scaling parameter set to -1σ value. First column gives recoil energies, subsequent columns give the values of $G'_i(E)$ for each of the 9 high-energy analysis bins. The sampling is in steps of 10 keV, which is too coarse to give an accurate signal model for very low WIMP masses, but is suitable for the mass range most relevant to our analysis. Higher resolution $G'_i(E)$ functions, and $G'_i(E)$ functions for other values of \mathcal{L}_{eff} , are given in supplementary material [give URL](#).

```

539
540 def TrapI(x,y):
541     """Simple trapezoid integration"""
542     w = x[1:] - x[:-1]
543     h = (y[1:] + y[:-1])/2.
544     return np.sum(w*h, axis=0)
545
546 # Load detector response table
547 data = np.loadtxt("detector_table.dat")
548 E = data[:,0]; Gi = data[:,1:]
549
550 # Load test recoil spectrum (1 TeV WIMP, 06)
551 data = np.loadtxt("06_1TeV.dat")
552 Er = data[:,0]
553 # Input spectra is normalised to coupling^2=1,
554 # rescale to something near limit (1e3)
555 # Also multiply in the appropriate exposure
556 dRdE = data[:,1] * (1e3/1.) * 224.6*34.
557
558 # Interpolate recoil spectrum to table values
559 # Assume spectrum zero outside data given
560 f_dRdE = interp1d(Er,dRdE)
561 dRdE_matched = f_dRdE(E)
562 Ri = TrapI(E[:,newaxis],Gi*dRdE_matched[:,newaxis])
563
564 for i,R in enumerate(Ri):
565     print "bin {0}: rate = {1:.2g}.".format(i+1,R)
566
567 Output:

```

```

568
569 bin 1: rate = 0.081
570 bin 2: rate = 0.098
571 bin 3: rate = 0.35
572 bin 4: rate = 0.46
573 bin 5: rate = 0.29
574 bin 6: rate = 0.22
575 bin 7: rate = 0.18
576 bin 8: rate = 0.47
577 bin 9: rate = 0.84

```

- 579 [1] David Harvey, Richard Massey, Thomas Kitching, Andy 624 [16] A. Liam Fitzpatrick, Wick Haxton, Emanuel Katz,
580 Taylor, and Eric Tittley. The nongravitational interac- 625 Nicholas Lubbers, and Yiming Xu. The Effective
581 tions of dark matter in colliding galaxy clusters. *Science*, 626 Field Theory of Dark Matter Direct Detection. *JCAP*,
582 347(6229):1462–1465, 2015. 627 1302:004, 2013.
- 583 [2] C. L. Bennett et al. Nine-Year Wilkinson Microwave 628 [17] David Tucker-Smith and Neal Weiner. Inelastic dark
584 Anisotropy Probe (WMAP) Observations: Final Maps 629 matter. *Phys. Rev.*, D64:043502, 2001.
- 585 and Results. *Astrophys. J. Suppl.*, 208:20, 2013.
- 586 [3] P. A. R. Ade et al. Planck 2015 results. XIII. Cosmolog- 630 [18] G. Barello, Spencer Chang, and Christopher A. Newby.
587 ical parameters. *Astron. Astrophys.*, 594:A13, 2016. 631 A Model Independent Approach to Inelastic Dark Matter
588 [4] J. Silk et al. *Particle Dark Matter: Observations, Models 632 Scattering. *Phys. Rev.*, D90(9):094027, 2014.*
589 and Searches. Cambridge Univ. Press, Cambridge, 2010.
- 590 [5] E. Aprile et al. XENON100 Dark Matter Results 633 [19] E. Aprile et al. The XENON100 Dark Matter Experi-
591 from a Combination of 477 Live Days. *Phys. Rev.*, 634 ment. *Astropart. Phys.*, 35:573–590, 2012.
- 592 D94(12):122001, 2016.
- 593 [6] Andi Tan and othrers. Dark matter results from first 635 [20] E. Aprile et al. Dark Matter Results from 225 Live Days
594 98.7 days of data from the pandax-ii experiment. *Phys. Rev.* 636 of XENON100 Data. *Phys. Rev. Lett.*, 109:181301, 2012.
- 595 *Lett.*, 117:121303, Sep 2016.
- 596 [7] D. S. Akerib et al. Improved Limits on Scattering of 637 [21] E. Aprile et al. Analysis of the XENON100 Dark Matter
597 Weakly Interacting Massive Particles from Reanalysis of 638 Search Data. *Astropart. Phys.*, 54:11–24, 2014.
- 598 2013 LUX Data. *Phys. Rev. Lett.*, 116(16):161301, 2016.
- 599 [8] C. E. Aalseth et al. Cogent: A search for low-mass dark 639 [22] E. Aprile et al. The neutron background of the
600 matter using *p*-type point contact germanium detectors. 640 XENON100 dark matter search experiment. *J. Phys.*,
601 *Phys. Rev. D*, 88:012002, Jul 2013. 641 G40:115201, 2013.
- 602 [9] R. Agnese et al. Search for low-mass weakly interact- 642 [23] E. Aprile et al. Response of the XENON100 Dark Matter
603 ing massive particles using voltage-assisted calorimetric 643 Detector to Nuclear Recoils. *Phys. Rev.*, D88:012006,
604 ionization detection in the supercdms experiment. *Phys.* 644 2013.
- 605 *Rev. Lett.*, 112:041302, Jan 2014.
- 606 [10] G.and others Angloher. Results from 730 kg days of the 645 [24] E. Aprile et al. Observation and applications of single-
607 cresst-ii dark matter search. *The European Physical Jour- 646 electron charge signals in the XENON100 experiment. *J.*
608 nal C*, 72(4):1971, 2012. 647 *Phys.*, G41:035201, 2014.
- 609 [11] R. Bernabei et al. New results from dama/libra. *The 648 [25] E. Aprile et al. Limits on spin-dependent wimp-nucleon
610 European Physical Journal C*, 67(1):39–49, 2010. 649 cross sections from 225 live days of xenon100 data. *Physi-*
611 [12] J. D. Lewin and P. F. Smith. Review of mathematics, 650 *cal review letters*, 111(2):021301, 2013.
- 612 numerical factors, and corrections for dark matter exper- 651 [26] Glen Cowan, Kyle Cranmer, Eilam Gross, and Ofer
613 iments based on elastic nuclear recoil. *Astropart. Phys.*, 652 Vitells. Asymptotic formulae for likelihood-based tests
614 6:87–112, 1996. 653 of new physics. *Eur. Phys. J.*, C71:1554, 2011. [Erratum:
615 [13] Spencer Chang, Aaron Pierce, and Neal Weiner. Mo- 654 *Eur. Phys. J.* C73,2501(2013)].
- 616 mentum Dependent Dark Matter Scattering. *JCAP*, 655 [27] E. Aprile et al. Dark Matter Results from 100 Live Days
617 1001:006, 2010. 656 of XENON100 Data. *Phys. Rev. Lett.*, 107:131302, 2011.
- 618 [14] A. Liam Fitzpatrick, Wick Haxton, Emanuel Katz, 657 [28] E. Aprile et al. Likelihood Approach to the First
619 Nicholas Lubbers, and Yiming Xu. Model Independent 658 Dark Matter Results from XENON100. *Phys. Rev.*,
620 Direct Detection Analyses. 2012. 659 D84:052003, 2011.
- 621 [15] Nikhil Anand, A. Liam Fitzpatrick, and W. C. Haxton. 660 [29] Alexander L. Read. Modified frequentist analysis of
622 Weakly interacting massive particle-nucleus elastic scat- 661 search results (The CL(s) method). In *Workshop on con-*
623 tering response. *Phys. Rev.*, C89(6):065501, 2014. 662 *fidence limits*, CERN, Geneva, Switzerland, 17-18 Jan
624 [30] K. Schneck et al. Dark matter effective field theory 663 2000: *Proceedings*, pages 81–101, 2000.
- 625 scattering in direct detection experiments. *Phys. Rev.*, 664 D91(9):092004, 2015.